Conserving elastic turbulence numerically using artificial diffusivity

V. Dzanic,[1] C. S. From,[2,*] and E. Sauret[1,†]

[1] *School of Mechanical, Medical, and Process Engineering, Faculty of Engineering, Queensland University of Technology, QLD 4001, Australia*

[2] *Department of Chemical Engineering, University of Manchester, Manchester M13 9PL, UK*

To simulate elastic turbulence, where viscoelasticity dominates, numerical solvers introduce an artificial stress diffusivity term to handle the steep polymer stress gradients that ensue. This has recently been shown [Gupta & Vincenzi, *J. Fluid Mech.* **870**, 405-418 (2019); Dzanic *et al., J. Fluid Mech.* **937**, A31 (2022)] to introduce unphysical artifacts with a detrimental impact on simulations. In this Letter, we propose that artificial diffusion is limited to regions where stress gradients are steep instead of seeking the zero-diffusivity limit. Through the cellular forcing and four-roll mill problem, we demonstrate that this modified artificial diffusivity is devoid of unphysical artifacts, allowing all features of elastic turbulence to be retained. Results are found to conform with direct simulations while only requiring a fraction of the numerical resolution.

It is well-known that fluid flow with the addition of polymer molecules to a solvent (i.e., viscoelastic fluids) in the absence of inertial instabilities $Re = \rho U \ell / \mu \leq 1$ generates an anisotropic elastic stress contribution that transitions the flow to a novel chaotic regime, known as elastic turbulence (ET) [1–3]. ET is purely driven by viscoelastic instabilities, where the viscous to elastic effects are measured by the Weissenberg number $Wi = \tau U / \ell \gg 1$, and viscoelastic and inertial effects characterized by the elasticity number $El \equiv Wi/Re = \tau\mu/(\rho\ell^2) \gg 1$. Here, τ is the longest polymer relaxation time, ℓ characteristic length scale, ρ is the density, μ is the total viscosity, and U is the average velocity. This purely elastic instability shares a lot of features with traditional inertial turbulence, namely, (i) increased flow resistance, (ii) enhanced mixing, (iii) random flow fluctuations characterized by a broadband spectrum of spatial and temporal frequencies [3]. In an effort to better understand the role of viscoelastic instabilities in these novel chaotic flow regimes, a plethora of numerical studies have been conducted [4–9]. The majority of which, involve resolving the hydrodynamic field through the incompressible Navier-Stokes equations,

$$\boldsymbol{\nabla \cdot u} = 0, \quad \frac{D\mathbf{u}}{Dt} = -\boldsymbol{\nabla} P + \mu_s \boldsymbol{\Delta \mathbf{u}} + \boldsymbol{\nabla \cdot \sigma} + \mathbf{F}, \tag{1}$$

coupled with the the polymer stress tensor $\boldsymbol{\sigma} = f(r)\frac{\mu_p}{\tau}(\boldsymbol{C} - \boldsymbol{I})$, described by a space-time dependent conformation tensor ($\boldsymbol{C}$) constitutive equation,

$$\frac{D\boldsymbol{C}}{Dt} = \boldsymbol{C} \cdot (\boldsymbol{\nabla \mathbf{u}}) + (\boldsymbol{\nabla \mathbf{u}})^{\mathsf{T}} \cdot \boldsymbol{C} - \frac{f(r)}{\tau}(\boldsymbol{C} - \boldsymbol{I}), \tag{2}$$

where the function $f(r)$ allows for various constitutive polymer models to be used. $\boldsymbol{I}$ is the identity tensor, $\mathbf{u}$ is the velocity field, $\mathbf{F}$ is the external force, μ_s and μ_p are the solvent and polymer dynamic viscosity, respectively.

Numerical simulations of turbulent viscoelastic fluid flows is, however, far from trivial. By definition, the conformation tensor is a symmetric positive-definite (SPD) tensor $\boldsymbol{C} \gtrsim 0$, where conserving this property is important to prevent the rapid growth of Hadamard instabilities [10]. To overcome stability issues, numerical methods apply decomposition techniques in Eq. (2) to conserve the SPD properties of $\boldsymbol{C}$ by construction [11, 12]. However, these specialized techniques alone cannot control the steep polymer stress gradients that ensue at high elastic effects, captured by the infamous high-Wi number problem, owing to the inherent hyperbolic nature and lack of numerical regularization terms in Eq. (2). In turn, solvers introduce an additional global artificial diffusivity (GAD) term in the Laplacian form, $\boldsymbol{D} = k\boldsymbol{\Delta C}$, into Eq. (2) [8, 9, 13], where the level of diffusivity k is characterized with respect to the solvent kinematic viscosity ν_s by the Schmidt number $Sc = \nu_s/k$. GAD effectively converts the constitutive polymer model to a parabolic form by smoothing steep polymer stresses over large regions of the flow. Indeed, polymer-stress diffusion is physically present at $Sc \sim 10^6$; however, to achieve numerical stability requires $Sc \lesssim 10^3$ [8, 14]. The unphysically large k values required to achieve such Sc numbers with GAD are known to promote laminarization for elasto-inertial turbulence (EIT) ($Re \gg 10$) [15], suppressing the elastic instabilities that are necessary to promote turbulence. By combining SPD-conserving solvers with high-order, shock-capturing schemes have enabled simulations of EIT without the need for GAD [16]. This same approach was recently used to simulate ET at $Sc = \infty$, where direct comparison against GAD with $Sc = 10^3$ revealed the dramatic effect on the large-scale properties of the flow, suppressing chaotic fluctuations [8]. In the authors' recent work [17], it was further shown that the global effect of GAD is so large that a single unit cell in fully-periodic problems does not conserve unicity, leading to numerical artifacts represented by qualitative anomalies, thus rendering the problem unphysical. Conserving unicity allows features of ET to be recovered at $Sc = 10^3$, with chaotic fluctuations increasing as $Sc > 10^3$, whereas ET is suppressed at $Sc \sim 10^2$, demonstrating the detrimental effect of GAD. Indeed in the absence of artificial diffusivity, an exact physical representation can be obtained directly from Eq. (2), however, for problems where $El \gg 1$, the steep

* christopher.from@manchester.ac.uk
† emilie.sauret@qut.edu.au

polymer stress gradients that develop require significant resolutions, and hence computational costs, to overcome the numerical stability issues that ensue [7, 8, 17].

In this Letter, a simple yet elegant approach to include artificially diffusivity while retaining all features of ET is proposed. We demonstrate the ability to avoid the unphysical artifacts that have plagued the GAD scheme while still offering the same level of numerical benefits, particularly in terms of convenience and stability.

Earlier works on turbulent polymer drag reduction have seen success using a local artificial diffusivity (LAD) scheme in which $\boldsymbol{D}(\boldsymbol{x},t) = k\boldsymbol{\Delta C}(\boldsymbol{x},t)$ is applied in regions of the computational domain $\boldsymbol{x}$ where $\boldsymbol{C} \leq 0$ [18, 19]. However, LAD does not guarantee SPD and is inherently not applicable to modern, SPD-conserving solvers [9, 11, 12]. Motivated by the LAD scheme and stability rationale, i.e., the singular purpose of artificial diffusivity is for numerical regularity, we seek a suitable approach with which k is not decreased but instead restricted where it is applied to minimize the potential consequent global effects. To this aim, we propose a modified artificial diffusivity (MAD) scheme such that $\boldsymbol{D}(\boldsymbol{x},t) = \kappa(\boldsymbol{x},t)\boldsymbol{\Delta C}(\boldsymbol{x},t)$ with $\max_{\boldsymbol{x}}[\kappa(\boldsymbol{x},t)] = k\ \forall t$, where $\boldsymbol{x}$ is the domain, which is directly applicable to all modern, SPD-conserving, numerical solvers. To illustrate, an intuitive way to apply κ is to consider the characteristic feature of ET, that the stress gradients are sharp and localised. By restricting artificial diffusivity within those regions to a maximum of $k = \nu_s/Sc$, we allow for the required numerical regularity to be retained while minimizing global smearing where regularization is not needed. Leveraging this idea, MAD considers the Laplacian form,

$$\boldsymbol{D}(\boldsymbol{x},t) = \frac{k\mathcal{Q}(\boldsymbol{x},t)}{\mathcal{Q}_{max}(t)}\boldsymbol{\Delta C}(\boldsymbol{x},t), \tag{3}$$

where $\mathcal{Q}$ is the sum of the magnitude of polymer stress component gradients, i.e.,

$$\mathcal{Q}(\boldsymbol{x},t) = \sum_{i,j}^{D}\sqrt{\sum_{q}^{D}\left[\nabla_q C_{ij}(\boldsymbol{x},t)\right]^2},$$

for a D dimensional domain $\boldsymbol{x}$ and $\mathcal{Q}_{max}(t) = \max_{\boldsymbol{x}}[\mathcal{Q}(\boldsymbol{x},t)]$ is a normalisation factor. In turn, in MAD (3) the artificial diffusivity is scaled linearly with stress gradients to a maximum of k, i.e., $\lim_{\mathcal{Q}\to\mathcal{Q}_{max}} \boldsymbol{D} = k\boldsymbol{\Delta C}$.

To demonstrate the suitability of the MAD scheme while further demonstrating the severe limitations of the GAD scheme for simulations of ET, we apply both MAD and GAD to simulate two popular ET cases, namely, the four-roll mill (FRM) problem [20–22] and the cellular forcing scheme (CF) [7, 8]. In recent investigations of ET, simulations of FRM and CF using GAD were shown to depict various numerical artifacts that have been investigated extensively in both [17] and [8], respectively, which presents strict test criteria for MAD. Both FRM and CF are numerical recreations of popular viscoelastic experimental cases [23–25], and are solved in a 2D domain

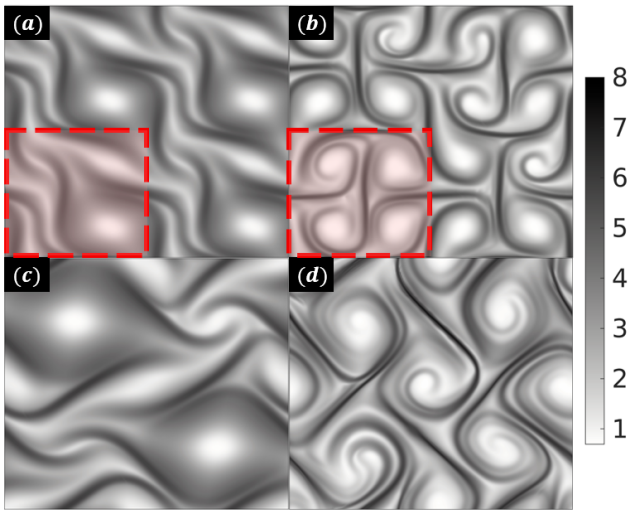

FIG. 1. Representative snapshots of $\ln(\mathrm{tr}\boldsymbol{C})$ for FRM (a,b) with $n = 2$ and CF (c,d) using GAD (a,c) and MAD (b,d). The red borders in (a,b) illustrate a single unit cell for FRM. For both cases, simulations with GAD (a,c) result in a loss of symmetry spawned from artificial diffusivity, whereas with MAD (b,d) they are largely constrained to the background forcing symmetry.

$\boldsymbol{x} = [0,\ n \times 2\pi]^2$ with double periodic boundary conditions (PBCs) where a single unit cell is $[0, 2\pi]^2$. Here, n is the level of periodicity, for which $n > 1$ results in n^2 unit cells to be solved. The experimental effect of rollers, which create an elongational flow regime, are mimicked through a constant external forcing, which for the FRM forcing scheme is given by

$$\mathbf{F}(\boldsymbol{x}) = F_0\left(2\sin(Kx)\cos(Ky),\ -2\cos(Kx)\sin(Ky)\right), \tag{4}$$

and for the CF forcing scheme,

$$\mathbf{F}(\boldsymbol{x}) = F_0\left(-\sin(Ky),\ \sin(Kx)\right), \tag{5}$$

in which the forcing amplitude is $F_0 = U\nu_s K^2$ and K is the spatial frequency (i.e., $\ell = 1/K$), resulting in a

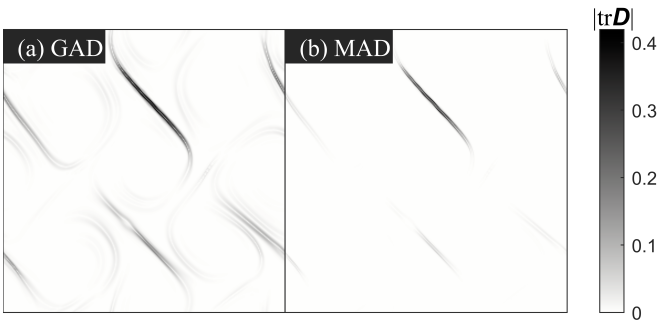

FIG. 2. The $|\mathrm{tr}\boldsymbol{D}|$ obtained with (a) GAD $\boldsymbol{D} = k\boldsymbol{\Delta C}$ and (b) MAD [Eq. (3)] using $\boldsymbol{C}$ from the simulation of CF with MAD in Fig. 1 (d). With MAD, $\boldsymbol{D}$ is largely concentrated at steep stress gradients where $\forall\kappa \gtrsim 0,\ Sc = 10^3 \sim 10^8$.

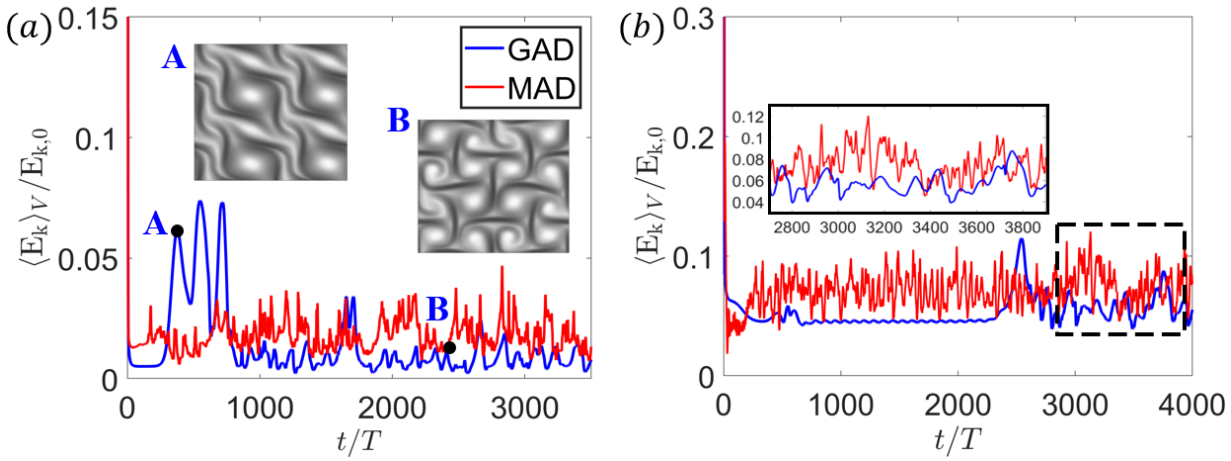

FIG. 3. Time series of the dimensionless mean kinetic energy $\langle E_k \rangle_V / E_{k,0}$ for the (a) FRM and (b) CF using the GAD (blue) and MAD (red) schemes. Note, insets provided in (a) correspond to the snapshots of $\ln(\mathrm{tr}\boldsymbol{C})$ at locations A ($t = 400T$) and B ($t = 2500T$) for the GAD scheme, illustrating the different transition points. The inset provided in (b) is a zoom-in corresponding to the late-time dynamics in the dashed box region.

turnover time $T = \nu_s K/F_0$. For FRM (4) $K = 1$ and for CF (5) $K = 2$. To simulate ET using FRM and CF, a small perturbation $\boldsymbol{\delta}$ is added to the initial conformation tensor $\boldsymbol{C} = \boldsymbol{I} + \boldsymbol{\delta}$, as originally proposed in [21]. Equations (1) and (2), with GAD and MAD (3), are solved using a SPD-conserving numerical solver comprising of the lattice Boltzmann coupled with a high-order finite-difference scheme (see [26]), which was applied in our previous investigation of ET [17]. We realistically capture the main physical behavior of polymers using the FENE-P constitutive model, $f(r) = \left(L^2 - 2\right) / \left(L^2 - r\right)$ in Eq. (2) with $r = \mathrm{tr}\left(\boldsymbol{C}\right)$ and $L^2 = 2.5 \times 10^3$, which imposes a maximum finite extensibility $L > r$ [27]. In all simulations, dimensionless groups are set following previous numerical investigations of ET including, $Wi = 10$, artificial diffusivity $Sc = 10^3$ (as done in [8, 21, 22]), and set $Re = 1$ (as done in [5, 7, 17]) below the critical value at which inertial instabilities arise $Re_c = \sqrt{2}$ [28]. The polymer concentration, characterized by $\beta = \nu_p/\nu_s$, is set to $\beta = 0.5$ and $\beta = 0.4$ in order to match previous investigations for FRM [21, 22] and CF[8], respectively.

Based on our previous investigation [17], GAD with $n = 1$ will result in unphysical artifacts arising from insufficient periodicity, characterized by qualitative anomalies which contaminate the base flow, thus preventing the accurate simulation of ET. For CF, we set $n = 1$ to compare against results from [8], which were solved on a $N^2 = 1024^2$ grid for both $Sc = 10^3$ (using GAD) and $Sc = \infty$. In addition, this is useful for testing whether unicity can be retained. For FRM, where the external forcing is larger, we set $n = 2$ to conserve unicity allowing numerical artifacts arising *purely* from artificial diffusivity to be studied. All simulations are purposely conducted with $(n \times N)^2 = 256^2$ grid points, where each unit cell has N^2 grid points, i.e., the resolution $2\pi/N$ for FRM is half of that used for CF. This is a notable reduction compared to previous studies [7, 8] to highlight the ability to retain numerical robustness with the proposed approach of modified artificial diffusivity.

In Fig. 1, contour plots of the polymer field $\ln(\mathrm{tr}\boldsymbol{C})$ using the GAD and MAD are compared for both the FRM [Fig. 1 (a) and (b)] and CF [Fig. 1 (c) and (d)] cases. The stark differences are immediately clear on a qualitative-scale. More specifically, it can be seen that FRM with GAD leads to a single-leading vortex within each unit cell [note, a unit cell is characterized by four rollers as illustrated by the red borders in Fig. 1 (a) and (b)], which appears during the onset of ET. Similarly, CF with GAD eventually transitions from the initial background forcing symmetry into a state with which dynamics are periodic and then into the double-leading vortices in Fig. 1 (c), where dynamics become aperiodic. Analogous results are obtained for FRM at $n = 1$ using GAD [21]. Ultimately, these are a product of the GAD excessively spreading polymer stresses over large regions of the flow, even within the vortical regions where there should be no polymer stretching, as illustrated in Fig. 2 (a). In turn, the polymer field eventually destabilizes and loses the initial forcing symmetry [8]. The initial breakdown in symmetry during the onset of ET has been shown to be independent of periodicity [17]. Furthermore, considering the same observations were made for CF with GAD [8] but at significantly larger resolution ($N^2 = 1024^2$) demonstrates the grid-independence of numerical artifacts arising from artificial diffusivity and periodicity. On the other hand, numerical simulations of FRM and CF with MAD are *devoid* of such numerical artifacts. For CF with MAD, despite experiencing momentary losses of symmetry, the polymer stretching is mostly constrained to the background forcing symmetry, in qualitative agreement with the results obtained using direct simulations at $Sc = \infty$ in [8] (see animations in the Supplementary

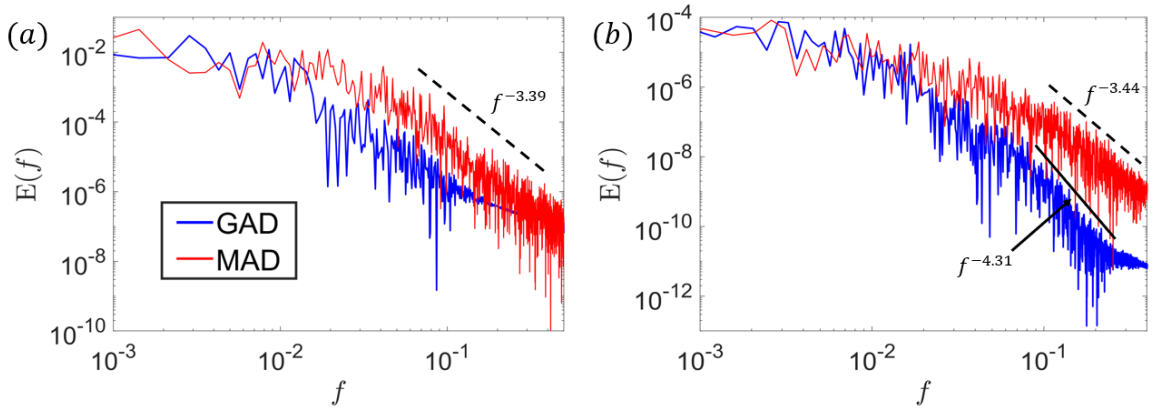

FIG. 4. The temporal power spectral density $E(f)$ of the dimensionless mean kinetic energy fluctuations for the (a) FRM and (b) CF using the GAD (blue) and MAD (red) schemes. Note, results with MAD follow a power law, $E \propto f^{-3.44}$ and $E \propto f^{-3.39}$ behavior for the FRM and CF cases, respectively. Alternatively, with GAD follows a steeper power law, $E \propto f^{-4.31}$ behavior for the FRM, while failing to follow a power law behavior for the CF.

Materials). Notably, the momentary losses of symmetry are expected to be eradicated with $n > 1$ [17], nevertheless, we shall see that these have a negligible impact on the ability to simulate ET. Essentially, MAD overcomes numerical artifacts by concentrating $\boldsymbol{D}$ only within the steep polymer stress gradients [Fig. 2 (b)], whereas with GAD $\boldsymbol{D}$ is diffused over all gradients [Fig. 2 (a)].

The quantitative results further reflect the stark differences observed for the two artificial diffusivity schemes. The time history response for the dimensionless mean kinetic energy $\langle E_k \rangle_V / E_{k,0}$, where $\langle \cdot \rangle_V$ denotes the spatial average and $E_{k,0} = U^2/2$, is shown for both FRM and CF in Fig. 3. Notably, the time series of the spatially-averaged polymer trace is also provided in the Supplementary Material and shows analogous results for both FRM and CF. In Fig. 3 (a), FRM with GAD initially reaches a steady-state, an artifact due to GAD suppressing intrinsic instabilities, followed by an onset of ET for which there is a rapid loss of symmetry [inset point A in Fig. 3 (a)], which is characterized by slow oscillations. In our previous study [17], we showed that a complex interplay exists between periodicity and artificial diffusivity, whereby the classic FRM problem, in which $n = 1$, is unable to overcome this initial loss of symmetry, as similarly observed for CF with GAD in Fig. 3 (b). Imposing sufficient n-levels of periodicity, as done here for FRM with $n = 2$, in turn, conserves unicity [e.g., the background forcing symmetry, shown in inset point B in Fig. 3 (a)] and enables features of ET to be recovered, such as chaotic flow fluctuations. Notably, defining $n > 2$ increases the rate at which ET is recovered after the initial loss of symmetry [17]. Remarkably, with MAD, the FRM results are devoid of all unphysical artifacts spawned from artificial diffusivity. When observing the results for CF with GAD in Fig. 3 (b), multiple instability modes exist. The first mode occurs within the early stages during an initial partial loss of flow symmetry, which periodically cycles between two different states, reflected by the fully periodic dynamics. This is the first observable numerical artifact caused by artificial diffusivity [8] and PBCs with limited periodicity [17]. Qualitatively, this instability mode can be appreciated in the animation provided in the Supplementary Materials. Beyond this state, the flow experiences a complete loss of symmetry, dominated by two vortices [refer to Fig 1 (c)] where the dynamics transition into an aperiodic state, as previously reported in [8] and analogous results can be observed for FRM with $n = 1$ [21, 22, 26]. While the initial loss of symmetry is a consequence of artificial diffusivity, the periodic and aperiodic states are largely due to the limited periodicity, where conserving unicity, as done here for FRM with GAD, prevents such unphysical behavior [17]. On the other hand, CF with MAD [Fig. 3 (b)] almost instantly transitions into a fully chaotic state, where the heavy fluctuations perturb the cellular vortices, however, the large-scale structure remains largely constrained to the background forcing with momentary losses of symmetry [refer to Fig. 1 (d)]. In comparing the late-time dynamics within the statistically homogeneous state (approximately $t > 500T$, for both FRM and CF), it is noticeable that for CF with MAD, fluctuations are at a much higher frequency compared to the slow aperiodic state observed for GAD. Similar observations were made in comparing GAD against the direct solution (i.e., $Sc = \infty$) [8]. Thus, the excessive diffusivity from GAD suppresses the chaotic fluctuations characteristic of the ET regime, a well-reported artifact of artificial diffusivity [8, 17]. High-frequency oscillations with MAD occur almost instantly for both FRM and CF, which is in agreement with the direct simulation of CF at $Sc = \infty$ [8] and experimental analog of FRM [25].

In Fig. 4, we examine the temporal power-law spectrum of the time signals from Fig. 3 within the statistically homogeneous regime. A distinctive feature of ET is a fairly steep power-law spectrum of velocity fluctuations [3, 29]. The fluctuations for FRM with $n = 2$ using GAD [Fig. 4 (a)] follows a steep power-law with an exponent of

$E \propto f^{-4.31}$. This steepness is independent of periodicity for $n \gtrsim 1$, [17] and the results here for FRM with MAD confirm this to be attributed to the numerical artifacts. The aperiodic state observed for CF with GAD [Fig. 4 (b)] fails to follow any apparent power law, as originally observed in [8] with significantly greater resolution. This is attributed to GAD suppressing the high-wavenumber fluctuations of polymer stresses and is analogously observed for FRM with $n = 1$ [17]. Ultimately, with GAD and $n = 1$, numerical simulations of FRM and CF are unable to conserve any features of ET. On the other hand, for both cases, the fluctuations retained in simulations with MAD behave as a power law, with exponents similar to previous experimental and numerical studies of ET, in which the decay rate varied with the setup, but the exponent was always smaller than -3 [1–3, 5, 29, 30]. The strong retention of ET features using MAD is a result of restricting artificial diffusivity within the critical regions of the flow [i.e., steep polymer stress gradients, as shown in Fig. 2], thus avoiding the consequent global deviation from the exact polymer representation (i.e., $Sc = \infty$). The remarkable feature of MAD is the numerical robustness while retaining all features of ET with an absence of numerical artifacts despite using 16 times less collocation points (i.e., a quarter resolution) compared to that required by direct simulations of ET at $Sc = \infty$ [7, 8].

Summarising, a new view on including numerical regularity for simulating ET through a modified artificial diffusivity (MAD) has been proposed. Its applicability is demonstrated by applying the MAD to two stringent numerical experiments. It is shown that with MAD, all characteristic features of ET can be simulated while overcoming the recently discovered unphysical numerical artifacts of the global artificial diffusivity used traditionally. The impact of artificial diffusion with MAD is effectively reduced from a qualitative scale to a quantitative scale, requiring a numerical grid that is one order of magnitude smaller compared to that required to numerically simulate ET at $Sc = \infty$. It is difficult to overlook the apparent trend and analogy that artificial diffusivity schemes share with traditional turbulence modeling. In a similar fashion, the MAD scheme is an additional numerical tool that offers numerical features that could be of paramount importance in progressing towards more complex and computationally expensive ET cases, notably, 3D simulations.

The authors acknowledge the High-Performance Computing facilities at QUT. Prof. E. Sauret is the recipient of an Australian Research Council Future Fellowship (FT200100446) funded by the Australian Government. V. Dzanic gratefully acknowledges QUT for support through a Ph.D. scholarship.

[1] A. Groisman and V. Steinberg, Nature **405** (2000), 10.1038/35011019.
[2] A. Groisman and V. Steinberg, New J. of Phys. **6** (2004), 10.1088/1367-2630/6/1/029.
[3] V. Steinberg, Ann. Rev. of Fluid Mech. **53**, 27 (2021).
[4] R. J. Poole, M. A. Alves, and P. J. Oliveira, Phys. Rev. Lett. **99**, 164503 (2007).
[5] S. Berti, A. Bistagnino, G. Boffetta, A. Celani, and S. Musacchio, Phys. Rev. E **77**, 055306 (2008).
[6] M. Grilli, A. Vázquez-Quesada, and M. Ellero, Phys. Rev. Lett. **110**, 174501 (2013).
[7] E. L. C. V. M. Plan, A. Gupta, D. Vincenzi, and J. D. Gibbon, J. of Fluid Mech. **822**, R4 (2017).
[8] A. Gupta and D. Vincenzi, J. of Fluid Mech. **870**, 405–418 (2019).
[9] M. Alves, P. Oliveira, and F. Pinho, Ann. Rev. of Fluid Mech. **53**, 509 (2021).
[10] R. Sureshkumar and A. N. Beris, J. of Non-Newtonian Fluid Mech. **60**, 53 (1995).
[11] T. Vaithianathan and L. R. Collins, J. of Comp. Phys. **187**, 1 (2003).
[12] R. Fattal and R. Kupferman, J. of Non-Newtonian Fluid Mech. **126**, 23 (2005).
[13] J. Lee, W. R. Hwang, and k. s. Cho, J. of Non-Newtonian Fluid Mech. **297**, 104650 (2021).
[14] T. Vaithianathan, A. Robert, J. G. Brasseur, and L. R. Collins, J. of Non-Newtonian Fluid Mech. **140**, 3 (2006).
[15] S. Sid, V. E. Terrapon, and Y. Dubief, Phys. Rev. Fluids **3**, 011301 (2018).
[16] A. Shekar, R. M. McMullen, B. J. McKeon, and M. D. Graham, J. of Fluid Mech. **897**, A3 (2020).
[17] V. Dzanic, C. S. From, and E. Sauret, J. of Fluid Mech. **937**, A31 (2022).
[18] T. Min, J. Yoo, and H. Choi, J. of Non-Newtonian Fluid Mech. **100**, 27 (2001).
[19] Y. Dubief, V. Terrapon, C. White, E. Shaqfeh , P. Moin, and S. Lele, Flow Turbul. Combust. **74**, 311 (2005).
[20] B. Thomases and M. Shelley, Phys. Fluids **19** (2007), 10.1063/1.2783426.
[21] B. Thomases and M. Shelley, Phys. Rev. Lett. **103**, 094501 (2009).
[22] B. Thomases, J. of Non-Newtonian Fluid Mech. **166**, 1221 (2011).
[23] O. Cardoso, D. Marteau, and P. Tabeling, Phys. Rev. E **49**, 454 (1994).
[24] D. M. Rothstein, E. Henry, and J. P. Gollub, Nature **401**, 770 (1999).
[25] B. Liu, M. Shelley, and J. Zhang, J. of Non-Newtonian Fluid Mech. **175-176**, 38 (2012).
[26] V. Dzanic, C. S. From, and E. Sauret, Computers & Fluids **235**, 105280 (2022).
[27] A. Peterlin, Polymer **2**, 257 (1961).
[28] K. Gotoh and M. Yamada, J. of the Phys. Society of Japan **53**, 3395 (1984).
[29] V. Steinberg, Phys. Rev. Lett. **123**, 234501 (2019).
[30] D. O. Canossi, G. Mompean, and S. Berti, Europhys. Lett. **129**, 24002 (2020).